

CRISM south polar mapping: First Mars year of observations

Adrian J. Brown ^{*1}, Wendy M. Calvin², Patrick C. McGuire³, Scott L. Murchie⁴

¹ *SETI Institute, 515 N. Whisman Rd, Mountain View, CA 94043, USA*

² *Geological Sciences, University of Nevada, Reno, NV, 89557, USA*

³ *McDonnell Center for the Space Sciences,*

Washington University in St. Louis, MO 63130, USA

⁴ *Johns Hopkins University Applied Physics Laboratory, Laurel, MD, 20723, USA*

* corresponding author, email: abrown@seti.org

Corresponding author:

Adrian Brown

SETI Institute

515 N. Whisman Rd Mountain View, CA 94043

ph. 650 810 0223

fax. 650 968 5830

email. abrown@seti.org

Short running title: "CRISM South polar mapping"

ABSTRACT

We report on mapping of the south polar region of Mars using data from the Compact Reconnaissance Imaging Spectrometer for Mars (CRISM) instrument. Our observations have led to the following discoveries:

1. Water ice is present in the form of pole-circling clouds originating from the circum-Hellas region, beginning prior to $L_s=162$ and diminishing markedly at $L_s=200-204$.
2. It has previously been inferred by temperature measurements (Titus et al., 2003) and $\text{CO}_2\text{-H}_2\text{O}$ mixture spectral models (Langevin et al., 2007) that surface water ice was present in the Cryptic Region in the final stages of sublimation. The high resolution of CRISM has revealed regions where only water ice is present (not a $\text{CO}_2\text{-H}_2\text{O}$ ice mixture). This water ice disappears completely by $L_s=252$ and may be the source of water vapor observed by CRISM in southern latitudes between $L_s=240-260$ (Smith, et al., this issue).
3. We have estimated surface CO_2 ice grain size distributions for the South Pole Residual Cap (SPRC) and the seasonal CO_2 ice cap that covers it throughout summer spring and summer. Our analysis suggests that grain sizes peak at $L_s=191-199$ with an apparent grain size of $\sim 7\pm 1\text{cm}$. By the end of the summer period our analysis demonstrates minimum apparent grain sizes of $\sim 5\pm 1\text{mm}$ predominate in the SPRC.
4. Fine grained CO_2 ice condenses from $L_s=0-40$, and extends symmetrically away from the geographic pole, extending beyond 80°S by $L_s=4-10$. No evidence for unusual CO_2 depositional processes in the Cryptic Region is observed up to $L_s=16$.

KEYWORDS

Mars, Polar regions, SPLD, cryptic region, CO_2 ice, H_2O ice, grain size

INTRODUCTION

Understanding the seasonal distribution of icy volatiles in the Martian polar regions is key to understanding the thermophysical balance of the Red Planet. The Viking Landers measured pressure variations of over 25% over a Martian year due to the sublimation and condensation of the polar caps (Hess et al., 1977; 1979; 1980). The pressure variations measured by the Viking Landers have been used to test heat budget models for the polar regions (Wood and Paige, 1992; Guo et al., 2009). Increasingly detailed sublimation timing information from the Thermal Emission Spectrometer (TES) instrument (Kieffer et al., 2000) and composition information from the THEMIS and OMEGA spectrometers (Titus, 2005b; Langevin et al., 2007; Piqueux et al., 2008) has led to greater appreciation for the complexity of the polar sublimation/condensation cycle.

This study extends the compositional investigation of the south polar sublimation cycle by presenting seasonal maps of icy volatiles, as observed by the CRISM on the Mars Reconnaissance Orbiter (MRO) spacecraft during its first Mars year in orbit. We also present contemporaneous mosaics of Mars Color Imager (MARCI) camera data.

In this study, we refer to timings using the terms MY for Mars Year, specified as starting on 11 April 1955 by Clancy et al. (2000). MY 28 began 22 Jan 2006, MY 29 began 10 December 2007. The term “ L_s ”, or solar longitude, refers to the celestial location of the sun when viewed from Mars (0-360°). This is a convenient measure of the Martian seasons – 180-360° is southern spring and summer. Aphelion occurs at $L_s=71^\circ$ and perihelion occurs at $L_s=251^\circ$.

Within this paper, we use the terms ‘grain size’ and ‘equivalent path length’ interchangeably – CRISM data cannot be used to derive actual grain sizes, but comparison of CRISM spectra with spectra generated by models can be used to deduce the average path length of light within a material before a scattering event, and this is used to infer a grain size by assuming scattering takes place at grain boundary intervals (Bohren, 1987).

CRISM

CRISM is a visible to near-infrared spectrometer sensitive to light with wavelengths from ~0.4 to ~4.0 μm (Murchie et al., 2007). CRISM is ideal for detecting hydrated minerals and ices (Brown et al., 2008a) because it covers unique spectral absorption bands in the 1-4 micron region. Previous thermal infrared observations of the Martian polar regions have been able to infer ice composition by the temperature of the surface (e.g. TES and THEMIS), however CRISM is able to determine ice composition by the presence of absorption bands. This enables the detection of pure phases and mixtures of CO_2 and H_2O ice. In addition, CRISM spectra can be used to derive ice grain sizes due to the

concomitant changes in absorption band strength with grain size, as discussed further below.

CRISM is the highest spatial resolution spectrometer to observe the Martian polar regions to date. In high-resolution mode, CRISM's instantaneous field of view or pixel size corresponds to ~18.75m on the ground. CRISM has 640 pixels in the cross-track direction, which corresponds to 12km on the surface of Mars, however only 605 pixels see the surface (edge pixels are intentionally blocked as calibration fiducials) therefore the swath width exposes ~10.8km on the ground.

In mapping mode (used in this study) 10x spatial binning is employed on the spacecraft, before data comes back to Earth. A mapping swath therefore is 64 pixels wide, each pixel being ~187.5m in the cross-track direction. Along-track binning is controlled by exposure time, which is variable by the type of observation, to keep pixels approximately square.

MARCI

The MARs Color Imager (MARCI) camera is a super wide angle, fish eye lens instrument with a 1024 pixels-wide CCD. Each Martian sol, MARCI obtains 12 continuous terminator-to-terminator, limb-to-limb color images, covering 60° of longitude. MARCI's seven bandpass filters are positioned at 260, 320 (UV), 425, 550, 600, 650 and 725nm(VIS). The UV channels have 7-8km resolution and the VIS channels just under 1km resolution (Malin et al., 2001).

METHODS

CRISM Seasonal mosaics

The seasonal mosaics discussed in this paper were constructed by collecting all the CRISM MSP (MultiSpectral Polar, which is a multispectral mapping mode for the polar regions) images acquired that extended south of 55° latitude for each two week MRO planning sequence.

In mapping mode, to keep data rates manageable, only a subset of the CRISM spectral bands are returned to Earth. MSP images have 19 bands in the CRISM 'S' (short wavelength, 0.36-1.0 μ m) and 55 bands in the CRISM 'L' (long wavelength, 1.0-3.9 μ m) detectors. In this paper, we have only used data from the 'L' detector, since it covers the absorption bands we require for mapping icy volatiles.

The images were mosaiced together using the "MR PRISM" software suite (Brown and Storrie-Lombardi, 2006) into a south polar stereographic projection with central meridian (longitudinal axis pointing directly down) of 180°, at a

resolution of 1000x1000 pixels (Figure 1). Each successive image that overlapped a previous image overwrote the previous data. No averaging of data took place during mosaic construction – the last pixel that was acquired in a region was the one that was used. Thus all the spectra in each prepared mosaic are unmodified spectra that were acquired at ~187.5m per pixel resolution.

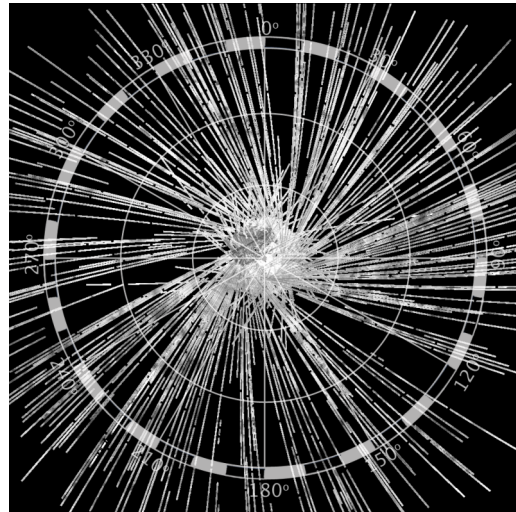


Figure 1. South polar mosaic of CRISM MSP images from Ls=295-003.

MSP observations were acquired on a best efforts basis, and conflicting requirements such as high data loads from other parts of the planet, solar conjunction and CRISM cooler swaps dictated that a variable number of MSP observations of the polar region were acquired in each two week period. The summary of south polar mapping observations for each MRO planning period is presented in Table 1.

MRO Planning Cycle	DOY (2007/08)	(MY) and L _s Range	S channel observations	L channel observations
6	(07)6-16	(28) 161.9-167.3	56	66
7	17-30	167.9-175.0	147	168
8	31-44	175.5-182.8	231	253
9	45-58	183.4-190.9	370	376
10	59-72	191.5-199.2	455	463
11	81-86	204.6-207.6	201	201
12	89-100	209.4-216.1	446	447
13	101-114	216.7-224.8	475	434
14	115-116	225.4-226.0	87	91
15	132-142	236.1-242.4	404	428
16	143-156	243.1-251.3	464	428
17	157-168	251.9-258.9	256	258
18	172-181	261.5-267.1	234	232
19	188-198	271.5-277.8	346	346
20	199-212	278.4-286.5	199	200
21	213-219	287.1-290.8	123	125
22	227-240	295.6-303.4	119	118
23	241-254	304.0-311.6	146	146
24	255-268	312.2-319.7	210	210
25	269-282	320.2-327.5	180	180
26	283-296	328.1-335.2	172	173
27	297-309	335.7-342.1	152	150
28*	350-352	(29) 3.1-4.1	26	26
29*	353-001	4.6-10.9	183	183
30*	(08)002-012	11.4-16.2	60	60
31*	016-026	18.1-22.8	35	35
32*	034-042	26.5-30.2	19	23
33*	044-044	31.1	2	2
34*	069-071	41.9-42.8	10	8

Table 1 - Number of CRISM MSP Strips taken of Mars southern pole (defined as all strips partially or completely poleward of 55°S) per fortnight (starting at cycle 6 of the MRO primary science mission) to July 17, 2007. Short channel is VNIR (0.4-1.0 μm) L channel is IR (1-4 μm). L_s = Deg of solar longitude. Southern spring starts at L_s = 180 and ends at L_s = 270. After (Brown et al., 2007). MY = Mars Year, L_s = solar longitude from Mars. MRO Planning cycles marked with an asterisk (*) are nominal - due to patchy coverage, we have amalgamated some cycles and omitted some.

All multispectral mapping images are acquired while CRISM is fixed in the nadir pointing direction.

The combination of field of view and instrumental constraints leads to the 'spaghetti strand' appearance of the resulting CRISM mosaics that are presented in this paper, with numerous gaps in surface coverage.

CRISM commenced imaging of the south polar region in January 2007, two months into the MRO mapping mission. This late start was due to the fact that CRISM requires sunlight to image the surface and until that time, the sun had not risen over the south polar region. CRISM multispectral mapping of the south pole was severely curtailed in mid-southern summer ($L_s=309$, MY 28) and finally halted on MY29 $L_s=16$ due to insufficient polar illumination.

Reduction of radiance to apparent reflectance

CRISM measures spectral radiance at sensor in $W.m^{-2}.sr^{-1}.\mu m^{-1}$. In order to retrieve the radiance value for each pixel, instrumental artifacts such as detector bias, electronic artifacts (bad pixels, ghosts, detector non-linearity), background subtraction (dark current), and stray light corrections are removed in the CRISM data processing pipeline (Murchie et al., 2007).

CRISM data is delivered by the instrument team to the Planetary Data System as radiance or I/F (radiance detected by the sensor ratioed to collimated flux power incident on the surface). Radiance at sensor is converted to I/F values by dividing the detected radiance by the solar flux at Mars (adopting symbology from Schott (1996)):

$$I/F = \frac{L_\lambda}{\left(\frac{\phi_\lambda}{\pi \cdot (r_{MARS})^2} \right)} \quad (\text{Eq.1})$$

where L_λ is the spectral radiance at sensor L in $Wm^{-2}sr^{-1}\mu m^{-1}$, ϕ_λ is the spectral solar flux at 1 astronomical unit (AU) in $Wm^{-2}\mu m^{-1}$ and r_{MARS} is the Mars-Sun distance in AU.

In order to retrieve apparent reflectance from the I/F data, we use the Digital Data Record supplied by the CRISM team to extract the solar incidence angle for each pixel in an observation and divide by the cosine of the incidence angle:

$$R = \frac{I/F}{\mu_0} \quad (\text{Eq.2})$$

where $\mu_0 = \cos(i)$, i is the solar incidence angle, 0° when the sun is overhead and 90° at the horizon.

Atmospheric effects

We used the term 'apparent reflectance' (used here with the symbol R) to indicate that time-variable atmospheric effects (scattering from dust and ice aerosols) have not been accounted for. This quantity is also sometimes termed 'lambert albedo' since it assumes isotropic scattering from the surface, however we prefer 'apparent reflectance' to emphasize no atmospheric correction has been applied to this data. All data used in this paper utilizes apparent reflectance values.

In the polar regions, over bright icy regions (surface albedos > 0.5), the effect of the atmosphere is minimal, due to the extremely thin nature of the Martian atmosphere and the strong reflectivity of CO_2 ice, particularly in the 1-4 μm region, and of H_2O ice, from 1-1.5 μm . Most of the ice identifications discussed in this paper are over bright, large grain CO_2 ice regions therefore the absence of an atmospheric correction does not prevent the identification of ices and the determination of CO_2 ice grain size.

There are two important cases where the atmosphere has an effect on the analysis discussed below. Those are the determination of the presence of clouds, and the variable opacity of dust aerosols. These are discussed as they are encountered in the relevant parts of the text.

CO_2 Ice Detection and Grain size Estimation Strategy

In order to construct the estimated CO_2 grain size maps for the seasonal mosaics, we removed a linear continuum between two specified shoulder points and then fitted a single Gaussian shape using an iterative least squares method similar to that described in Brown (2006). We used the depth of the inverted Gaussian shape to evaluate the grain size by comparison with a spectral model.

We used two diagnostic absorption bands to determine the presence and abundance of CO_2 ice. These bands are centered at 1.435 μm (shoulder points at 1.38 and 1.47 μm) and 2.28 μm (shoulder points at 2.2 and 2.4 μm). The 1.435 μm band was used to prepare maps of CO_2 ice presence, and the 2.28 μm band was used to estimate the grain size. The 2.28 μm band is able to give a more accurate grain size estimate because 1.) it is not obstructed by CO_2 atmospheric absorption bands and 2.) it is not overlapped by similar size H_2O ice absorption bands (Calvin and Martin, 1994).

To link the depth of the absorption band to a grain size, we constructed a range of spectral models using the Shkuratov (1999) surface particulate spectral reflectance model. The Shkuratov surface model is a simple geometrical optics (ray tracing) model that converts optical constants into the expected reflectance of a particulate surface, given a monodisperse grain size distribution (all grains the same size) and porosity. The model is one-dimensional and treats the

powder as a stack of slabs of width equal to the grain size, and with holes in the slabs to represent the porosity. It has been used previously to retrieve the grain size of ices in the Martian south polar region (Langevin et al., 2007). We used the optical constants of solid CO₂ ice as derived by Hansen (1997; 2005). All band depth calculations were conducted on spectra that had been convolved to the CRISM multispectral wavelengths. All mixtures were performed at the full resolution of the optical constants (roughly 0.2nm in the 1-4µm range) before convolution to CRISM multispectral wavelengths.

CO₂ snowpack density and porosity estimation. Several studies have derived the density of the Martian CO₂ seasonal deposits, with particular emphasis on the north pole seasonal deposits. Solid CO₂ has a density of 1606 kg m⁻³. Smith et al. (2001) used combined MOLA gravity/elevation measurements to derive a density of 910±230kg.m⁻³ for the north pole. Feldman et al. used the Gamma Ray Spectrometer (GRS) on Mars Odyssey to derive a density of 910 kg m⁻³ (Feldman et al., 2003). Titus et al. suggest that the south polar seasonal cap density is probably around 1000 kg m⁻³. Guided by these estimates, we adopt a porosity of 60% for our CO₂ ice spectral models. A constant density is unlikely to be realized in nature, but one value needs to be chosen for consistent results.

In Figure 2.1a, we plot the depth of the 1.435µm absorption band against the modeled CO₂ ice grain size, using Shkuratov's surface reflectance method with an assumed porosity ('q' in Shkuratov's terms) of 0.1, 0.6 and 1.0.

In Figure 2.1b, we plot the relative band depth of the 2.28µm absorption band, also determined using Shkuratov's surface reflectance model for pure CO₂ ice. This figure presents the relationship we used to infer CO₂ grain sizes from CRISM reflectance measurements. To give an estimate of how the grain size retrieval is affected by Shkuratov's porosity parameter, we have also plotted the relative band depth vs. grain size for a porosity of 0.1 (extremely fluffy snow) and 1.0 (slab ice) bracketing the possible extremes we might encounter.

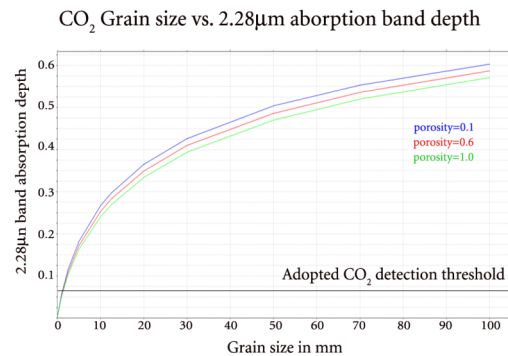


Figure 2.1b. Modeled relationship of particulate CO₂ ice 2.28 µm absorption band depth versus grain size for porosity of 0.1, 0.6 and 1.0. The adopted CO₂ detection threshold of 0.07 is shown.

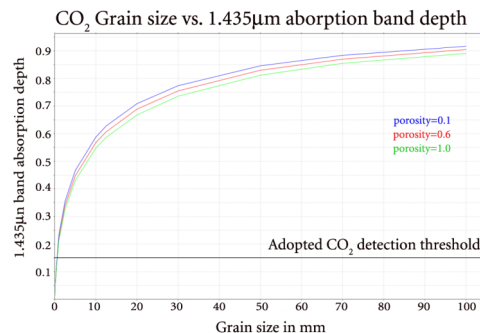


Figure 2.1a. Modeled relationship of particulate CO₂ ice 1.435 µm absorption band depth versus grain size for porosity = 0.1, 0.6 and 1.0. The adopted CO₂ detection threshold of 0.16 is shown.

For CO₂ ice with a grain size of 5mm, the variation between porosity extremes is ±1mm, for grain sizes of 30 mm, ±3mm and for grain size of 80mm, the variation is ±9mm. Therefore the unknown porosity of the ice introduces a relatively large (up to ±10%) uncertainty into our grain size derivation. This is the largest source of error in our calculations. CRISM SNR at 2.28μm is ~400 and contributes a worst case error for a 2.28μm band depth of 0.08 of (1/400)/0.07=3.5%. If we assume the porosity error and instrumental noise are independent errors, and convolve them according to $total\ error = \sqrt{errorA^2 + errorB^2}$ then the worst case instrumental error adds ~0.6% to the porosity error. Therefore we use ±10% (rounded up to 1 significant digit) as our error estimate when quoting grain sizes in the Observations section below.

In order to create the interpretive ice maps for the seasonal mosaics, we used the 1.435μm CO₂ absorption band depth to 'detect' the presence of CO₂ ice. During testing with a range of threshold values, we found CO₂ gas absorption in the Martian south polar atmosphere tops out at relative band strength of ~0.15 at 1.435μm. Therefore, to detect CO₂ ice without spurious atmospheric detections, we chose to use a threshold value of 0.16 for the relative strength of this absorption, as indicated on Figure 2.1a. According to our models, this leads to a lower detection limit of pure CO₂ grains of approximately 750 microns in size. In comparison, the OMEGA team used a threshold of 0.2 (Langevin et al. (2007), para. [47]).

In order to estimate CO₂ grain sizes, the relative band depth at 2.28μm was used in conjunction with the optical model discussed previously (Figure 2.1b). We found that a lower threshold of 0.07 (shown as a horizontal line) eliminated non-CO₂ ice returns, which translates to a lower threshold of pure CO₂ grains about 1200 microns in size. This threshold was chosen to prevent noisy spectra being misidentified and put into the relative band depth histograms.

Linear and intimate mixtures with soil and dust. Grain sizes indicated by the mosaics will be inaccurate when CO₂ does not cover the entire pixel (~187.5m across) or if the CO₂ ice is not 'optically thick'. If CO₂ does not cover the entire region, the grain sizes will be underestimated. This effect will be most prevalent on the edges of the CO₂ cap. To illustrate the effect of impurities on the derivation of CO₂ ice grain size, we have prepared linear and intimate mixing models of CO₂ ice with palagonite, which is a 'dust' or 'dirt' representative that is often used for Martian soil (Brown et al., 2008a).

Linear mixing assumes that light reflect by one component does not interact with the other component before detection by the sensor. This approximates the situation where two components are side by side within one pixel. In the intimate mixing model, light reaching the sensor has bounced many times between the two components.

Linear mixtures of CO₂ ice and soil. We prepared a linear spectral model that point-by-point averages Shkuratov-derived reflectance spectra from two components – CO₂ ice with grain size of 2.5 mm and a porosity of 0.6 and palagonite with a grain size of 100 microns and porosity of 0.6. Figure 2.1c shows the results of employing our model with different linear mixture ratios, and calculating the 2.28 μm band depth to determine the grain size (by assuming the relationship in Figure 2.1b). As can be determined from the graph, the relationship between inferred grain size and mixing ratio is not linear, in fact, the partial coverage of the CO₂ ice must drop to less than 60% before the grain size estimate decreases to 80% of its true value.

Intimately mixed dust and CO₂ ice. The assumption of pure CO₂ ice is not likely to be realized on the south polar cap, since it is likely that small amounts of ‘dust’ or darker material will be intimately mixed in with the CO₂. For example, Doute et al. (2006) estimated that the ‘typical’ SPRC CO₂ ice had dust contents of 0.03-0.06% and were 99.9% CO₂ ice. It has been shown that even such a small amount of dust intimately mixed in with CO₂ ice will decrease the band depth and lead to a decrease in grain size estimation (Kieffer, 1990; Calvin and Martin, 1994). To illustrate the effect of intimate mixing on the derived grain sizes, we have used the Shkuratov coarse grain intimate mixing model (his equation 14) and the same CO₂ ice grains (2.5 mm, porosity=0.6) and palagonite grains (100 microns, porosity=0.6) as used in the linear mixing model, and plotted the results on Figure 2.1c. As can be seen, intimate mixtures have a much stronger effect on the albedo (and hence the inferred grain sizes) than linear mixing. Mixing CO₂ ice (2.5mm grain size) intimately with palagonite (100 microns grain size and a volume amount of 0.05) will result in the grain size of the CO₂ ice grain size being estimated at 1.8mm, a 30% error.

Our models of linear and intimate mixing of impurities with CO₂ ice show that impurities reduce the apparent grain size, and this is why we use the term ‘minimum apparent’ grain sizes when describing our findings.

CO₂ Ice Clouds. Assuming ice particles in the polar regions are not replenished and follow the Stokes-Cunningham settling model, 10μm grain sizes are likely to have an atmospheric residence time of around 10 hours, and therefore grains larger than 10μm are likely to fall to the surface in the thin Martian atmosphere (Conrath, 1975). Since persistent CO₂ ice clouds should have particle sizes of less than 10μm and our method of detecting CO₂ ice involves thresholds that eliminate sensitivity to very fine grained (<1mm) CO₂ grains,

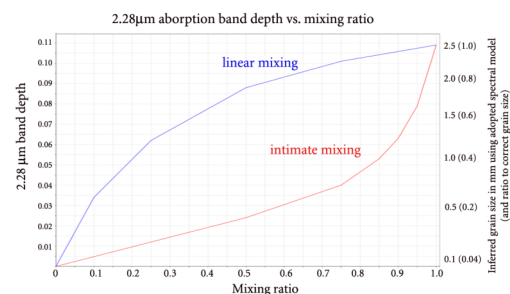


Figure 2.1c. Linear vs. intimate mixing. Modeled relationship of particulate CO₂ ice 2.28 μm absorption band depth versus mixing ratio when CO₂ ice of grain size 2.5mm is mixed with palagonite of grain size 100 microns. Porosity of all components is 0.6. Linear mixing is in blue, intimate mixing in red. Incorrectly inferred grain sizes using the standard spectral model used in this study are plotted on the right axis.

our CO₂ index maps are not sensitive to CO₂ ice clouds. CO₂ ice clouds have been suggested to form in the polar night when atmospheric temperatures are cold enough for CO₂ ice to condense (Hinson and Wilson, 2002). MOLA echoes during the polar night have been interpreted as returns from convective CO₂ ice clouds (Pettengill and Ford, 2000; Colaprete and Toon, 2002; Tobie et al., 2003). Recent SPICAM solar occultation observations have been interpreted to result from the presence of noctilucent CO₂ ice clouds at ~100km with grain sizes of ~100nm (Montmessin et al., 2006). If CO₂ ice clouds only form during the polar night, they will not be visible in the CRISM MSP dataset, which was collected when the surface is illuminated.

H₂O Ice Detection Strategy

In order to detect water ice, we used a water ice index similar to that suggested by Langevin et al. (2007), adjusted to accommodate CRISM multispectral mapping bands. The CRISM adjusted MSP H₂O index formula is:

$$H_2O_{index} = 1 - \frac{R(1.500)}{R(1.394)^{0.7} R(1.750)^{0.3}} \quad (\text{Eq. 3})$$

where $R(\lambda)$ is the apparent reflectance at wavelength λ in microns. Langevin et al. (2007) used wavelengths at 1.385 and 1.772 μ m in the denominator, and for comparison with their work we have approximated this relationship as closely as possible.

As for the CO₂ index threshold, we generated maps of water ice using a range of different thresholds and checked by hand how many incorrect or dubious water identifications were made for each threshold. We required that the H₂O 1.5 μ m absorption band had to be readily apparent above CRISM noise. CRISM has a nominal SNR of ~400 in this region of the spectrum (Murchie et al., 2007) however the achieved SNR will be adversely affected by the low-light conditions in the south polar MSP dataset. We adopted a H₂O index threshold of 0.125 since this value removed random noise from our H₂O detection maps.

Model to test H₂O index threshold. To estimate how much water ice is detectable with an adopted H₂O index of 0.125, we created a spectral model of a CO₂ snowpack with embedded (intimately mixed) H₂O grains. The grain sizes chosen have been guided by the results of previous research (Kieffer et al., 2000; Glenar et al., 2005; Doute et al., 2006; Langevin et al., 2007) but are only intended as a basic plausible model rather than a real physical situation. We

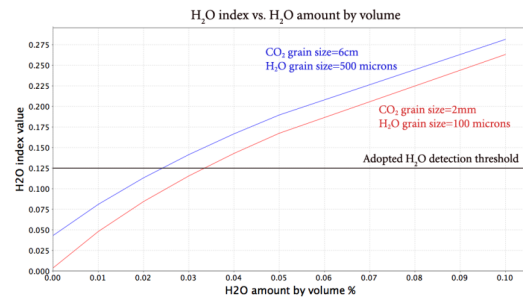


Figure 2.2a. Modeled relationship of particulate H₂O ice index (Equation 3) versus modeled water amount by volume (in the presence of CO₂ grains 2mm in size).

used the Shkuratov (1999) intimate mixture particulate model (his equation 14) to generate approximate spectra of CO₂ mixed with water ice. We assumed a two component intimate mixture of porosity 0.6, with CO₂ ice grain size of 60000 microns and a water ice grain size of 500 microns (guided by the Doute et al. (2006) best fit to ‘typical Bright residual cap’) and varied the water amount by volume from 0 to 0.05. We then repeated this calculation series for CO₂ ice grain size of 2000 microns and a H₂O ice grain size of 100 microns (more typical of what we observe in the seasonal cap or Cryptic Region). The mixing calculations were done at full spectral resolution of the optical constants and the H₂O index calculated after convolution to MSP wavelengths. The results of this modeling are shown in Figure 2.2a.

This simple spectral model gives some idea of the sensitivity of the H₂O index for plausible H₂O and CO₂ mixtures. As can be seen in the figure, this simple model suggests that using our chosen threshold, for the chosen range of CO₂ and H₂O ice grain sizes, the water ice will be detected when it is present in amounts greater than 2.5-3.5% by volume.

H₂O index Modeling assumptions. The caveats discussed above for our CO₂ ice spectral modeling also apply to our H₂O ice spectral modeling. Our modeling implicitly assumes H₂O and CO₂ are intimately mixed on the surface, however as will be shown later, it is probable that some of the H₂O ice we detect is in the form of water ice clouds, and our intimate mixture models are not expected to perform adequately when this situation exists. Another situation that our intimate mixing model will not simulate is cold trapped H₂O molecules forming layers over a CO₂ substrate. In this layered configuration, it is likely that CO₂ absorption features will be suppressed even further than in the intimate mixing situation, and smaller amounts of H₂O (i.e. even less than 2.5% as quoted above) may be detectable.

H₂O ice grain size estimation. Langevin et al. (2007) suggested a ratio of the 3.4/3.525 μ m bands of OMEGA would enable the detection of water ice clouds, since they made the assumption that small water ice grain sizes correspond to water ice cloud (Langevin et al. (2007), para [32]). To use this method with our CRISM dataset, we created a similar index, using the 3.397 μ m and 3.503 μ m CRISM bands, since these are available in the MSP spectral subset.

$$H_2O_{grainSizeIndex} = \frac{R(3.397)}{R(3.503)} \quad (\text{Eq. 4})$$

In order to justify the use of this ratio for detection of fine grained water ice, we created a simple, one component Shkuratov-based spectral model using H₂O ice of porosity 0.6 and varying grain size. The results are shown in Figure 2.2b, for both the Langevin index and the slightly less effective modified CRISM index. It can be seen that the spectral factor behind the effectiveness of the 3.4/3.525 μ m ratio is the peak at 3.8 μ m. This peak is present in small grains (< 50 microns) but decreases in size and eventually disappears for grains larger than 50 microns. Langevin et al. (in para [32]) suggest the 3.4/3.525 μ m index might be used to discriminate between grains of mm to cm, however we contend that its usefulness decreases markedly for grains larger than 50 microns. As Langevin et al. noted (in their para [32] and caption for their Figure 30), the index can be confused in the presence of large grained CO₂ ice due to overlapping of absorption bands. In addition, the SNR for CRISM in the 3-4 μ m region drops below 100 (Murchie, 2007). These two factors make interpretation of the H₂O ice grain size ratio challenging.

Assuming, as discussed earlier for CO₂ ice clouds, that persistent water ice clouds are likely to have grain sizes around 10 microns and definitely smaller than 50 microns, therefore we consider a 3.397/3.503 ratio value of less than 0.6 to be due to fine grained ice, and potentially persistent water ice cloud.

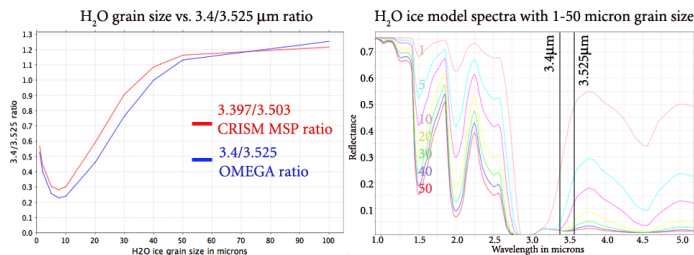


Figure 2.2b. (left) Plot of H₂O ice grain size index (Equation 4) versus modeled water ice grain size and (right) model water ice spectra with grain sizes from 1-50 microns, vertical lines show the ratio points.

CROCUS Line Mapping

Despite the sometimes sparse CRISM mapping coverage of the polar regions it is possible to obtain an estimate of when the Cap Recession Observations indicated CO₂ has Ultimately Sublimated (CROCUS line - which corresponds to the retreating seasonal cap (Kieffer et al., 2000)) for comparison with previous studies (James et al., 1987; Kieffer et al., 2000; Titus, 2005a; Piqueux and Christensen, 2008).

In this study, we calculated the CROCUS line using the icy volatile mosaics. We defined the edge of the retreating cap as the location where CO₂ or CO₂+H₂O was found, furthest away from the south pole. Due to the patchy nature of CRISM MSP coverage, we used a computer algorithm to automatically recognize the edge of the cap by laying down transects away from the pole, and finding the point along that transect where the last CO₂ or CO₂+H₂O point was mapped (using the thresholds defined previously). In order to avoid outliers or spurious noise, for positive detection of the cap edge we required that the pixel in question be surrounded by five adjacent pixels that were also mapped as containing CO₂

or CO₂+H₂O ice. We used linear interpolation to jump over areas of missing data. We used a variable lookahead scheme to look for the next point with the greatest radius away from the south pole.

MARCI Daily mosaics

The MRO orbit is 117 minutes long, and over the course of the 12.6 MRO orbits per Martian sol, MARCI maps out a set of swaths under the spacecraft ground track. These swaths are mosaiced at Malin Space Science Systems into a cylindrical projection “Daily Global Map” (DGM) product. We use this DGM product, re-projected to south polar stereographic orientation to 60°S latitude, and replacing the green channel with an average of red and blue to provide a better approximation of Martian surface color. The DGMs include a photometric correction averaging over the past several martian sols. This correction imparts a dark ring, coincident with the farthest outlier of bright ice material, particularly evident in the later L_s images in Figure 3 (see e.g. L_s=260.2 in Figure 3.4 – the dark core is an artifact of the processing technique). These images are not accurate apparent radiance products, but provide confirmation at improved spatial fidelity of the seasonal ice mapping provided by CRISM. Camera acquisitions are automatically keyed to season so that data strips do not always cover the geometric pole and this results in dark gores at the center of the images at both early and late L_s values. Obscuration by the MY28 large global dust event is particularly evident from L_s=270-304. Off-axis observations for other instruments also impart gores in the DGMs. These are observed as either missing data or areas along the mosaic seams where the color bands do not perfectly line up so that there are blue, orange or white color artifacts along some radial strip boundaries. For each CRISM time period we have selected the best corresponding DGM image with the fewest artifacts.

OBSERVATIONS

Seasonal mosaics

Figure 3 shows the seasonal mosaics of CRISM, alongside MARCI data for taken within the same time period.

A variable number of CRISM MSP observations was taken per two week cycle, this number is indicated as '*n*' on the left hand side of the images. In the final Figure (Figure 3.7) since the observations are so few, these have been lumped into periods greater than the two week MRO planning cycle. Where the indicated period is less than two weeks, it has been shortened to include the period when the earliest and latest CRISM image was acquired in that cycle.

<these figures are too large so they are available on the web at these links:>

<http://abrown.seti.org/research/downloads/brown-jgr-crisp-sth-pole-my-28/figure3.1.png>

Figure 3.1. South polar seasonal mosaics for period from MY 28 Ls=160-191. (left) Daily MARCI mosaic. (center) CO₂ 1.435 μm absorption depth (right) Ice identification maps

<http://abrown.seti.org/research/downloads/brown-jgr-crisp-sth-pole-my-28/figure3.2.png>

Figure 3.2. South polar seasonal mosaics for period from MY 28 Ls=191-225. (left) Daily MARCI mosaic. (center) CO₂ 1.435 μm absorption depth (right) Ice identification maps

<http://abrown.seti.org/research/downloads/brown-jgr-crisp-sth-pole-my-28/figure3.3.png>

Figure 3.3. South polar seasonal mosaics for period from MY 28 Ls=225-260. (left) Daily MARCI mosaic. (center) CO₂ 1.435 μm absorption depth (right) Ice identification maps

<http://abrown.seti.org/research/downloads/brown-jgr-crisp-sth-pole-my-28/figure3.4.png>

Figure 3.4. South polar seasonal mosaics for period from MY 28 Ls=260-290. (left) Daily MARCI mosaic. (center) CO₂ 1.435 μm absorption depth (right) Ice identification maps

<http://abrown.seti.org/research/downloads/brown-jgr-crisp-sth-pole-my-28/figure3.5.png>

Figure 3.5. South polar seasonal mosaics for period from MY 28 Ls=290-330. (left) Daily MARCI mosaic. (center) CO₂ 1.435 μm absorption depth (right) Ice identification maps

<http://abrown.seti.org/research/downloads/brown-jgr-crisp-sth-pole-my-28/figure3.6.png>

Figure 3.6. South polar seasonal mosaics for period from MY 28 Ls=330 to MY29 Ls=10. (left) Daily MARCI mosaic. (center) CO₂ 1.435 μm absorption depth (right) Ice identification maps

<http://abrown.seti.org/research/downloads/brown-jgr-crisp-sth-pole-my-28/figure3.7.png>

Figure 3.7. South polar seasonal mosaics for period from MY 28 Ls=10 to MY 29 Ls=40. (left) Daily MARCI mosaic. (center) CO₂ 1.435 μm absorption depth (right) Ice identification maps

Figure 4 shows representative spectra of different spectral classes at different points and times in the south polar cap taken from the MSP dataset. The spectral differences between CO₂ ice and gas absorptions can be appreciated by comparing Figure 4.a to Figure 4.f. The difference between fine grained and coarse grained CO₂ ice can be seen in Figure 4.a and 4.b, and for fine and coarse grain H₂O ice comparison can be made between Figures 4.c and 4.d. Note that “fine” and “coarse grain” spectra for CO₂ ice and H₂O ice correspond to physically different size grains.

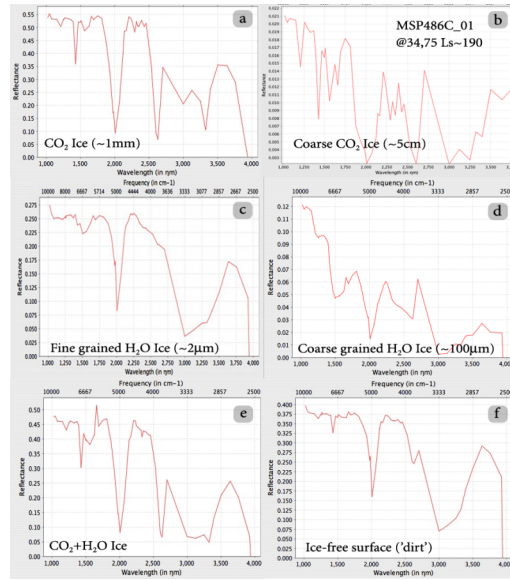


Figure 4. Representative spectra of spectral classes taken from the MSP dataset. See text for discussion. Reflectance here is “apparent reflectance” (incidence angle corrected) as discussed in the text and no atmospheric correction has been carried out. Note the subtle effect of H₂O ice on CO₂ ice (in Figure 4.e there is a slight decrease in reflectance at 1.5µm relative to Figure 4.a)

CROCUS lines and Cap Area

Figure 5 plots the CROCUS line (defined here as the boundary of CO₂ ice as detected by the seasonal mosaics and determined by the threshold in figure 2.1) as a function of time. Due to our interpolation method which is required to skip areas of missing data, the edge of the cap is unrealistically simplified, however our results are similar to observations on previous years (James et al., 1979; James et al., 1987; Kieffer et al., 2000; Benson and James, 2005; Titus, 2005a; Giuranna et al., 2007; James et al., 2007; Piqueux and Christensen, 2008).

Using the polygons in Figure 5, we are able to estimate the surface area of the cap. We use a method of computing the area of an irregular polygon supplied by the publicly available Computational Geometry Algorithms Library (CGAL). Figure 6 plots the estimate of the area of the seasonal cap and the rate of change in the area of the cap per 24hrs versus solar longitude. The rate of change of the cap area averages around 52,000 km² per day from L_s=168 to L_s=310 and peaks at just under 110,000 km² per day at L_s=225.

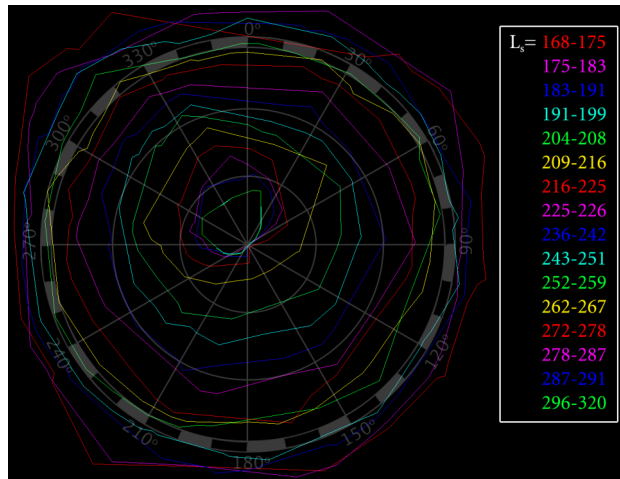


Figure 5. CO₂ seasonal cap edge (CROCUS) lines for MY28 L_s=168-320.

Assuming CO₂ mass load of 700 kg.m⁻², as measured by GRS (Feldman et al., 2003) during peak sublimation times at L_s=225, 7.7x10¹³ kg of CO₂ is sublimed into the atmosphere per day.

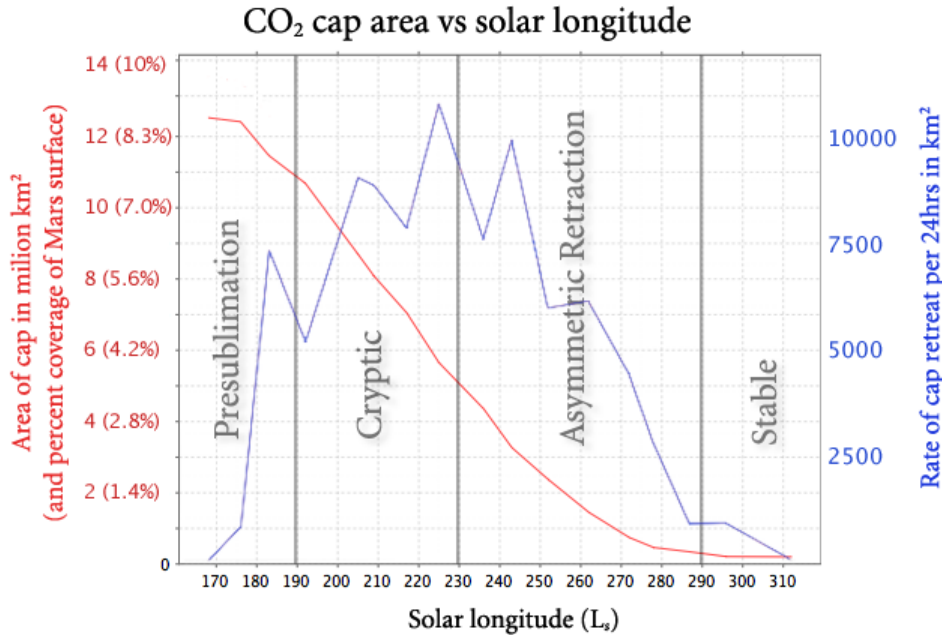


Figure 6. CO₂ seasonal cap area for L_s=168-312 (in red) and cap rate of retreat in km² per 24 hours (in blue). Sublimation phases indicated are discussed in the text.

Histograms of seasonal CO₂ ice grain size

Figures 7.1-7.5 show the seasonal histograms of derived CO₂ grain sizes derived from the CRISM mosaics.

The histograms have been constructed using the relative band strength of the 2.28μm CO₂ ice feature. All spectra that exhibited a relative band depth threshold of 0.07 were classed as CO₂ ice spectra, and included in the histogram data. All other spectra (not containing CO₂ ice) were omitted from the histograms. The spectra were binned into 1 of 100 bins according to their relative band depth. Each bin was summed to create the histogram, and then each bin was normalized according to the number of CO₂ ice pixels found in each two week mosaic.

The histograms include data from periods matching the MRO planning cycle, from L_s=162-016, corresponding to the mosaics in Figures 3.1-3.7. Each histogram has been grouped to reflect the different stages of the springtime recession (pre-sublimation, cryptic, asymmetric recession, stable and recondensation periods). Due to the small number of pixels available for analysis, we show only two histograms in the recondensation period (L_s=4.6-10.9 and 11.4-16.2).

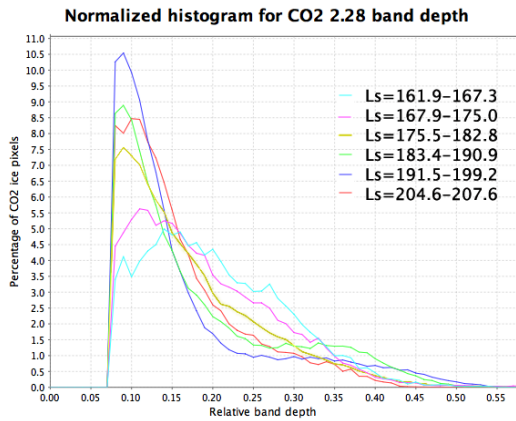


Figure 7.1 Histograms showing CO₂ surface ice grain size distributions for the Presublimation period corresponding to six MRO planning cycles used to prepare Figure 3 mosaics.

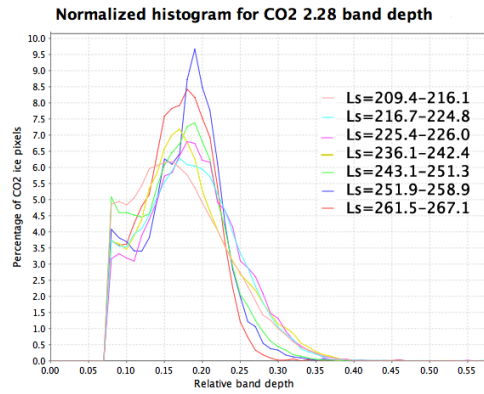


Figure 7.2 Histograms showing CO₂ surface ice grain size distributions for the Cryptic period corresponding to seven MRO planning cycles used to prepare Figure 3 mosaics.

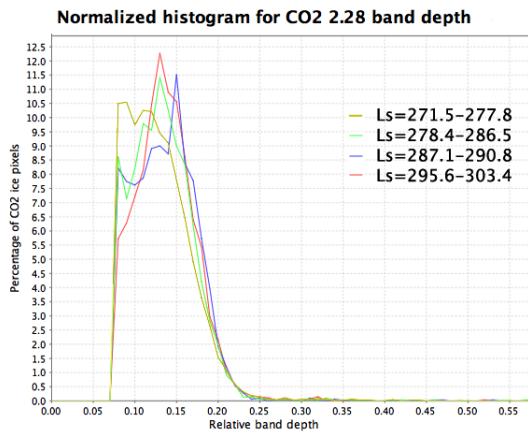


Figure 7.3 Histograms showing CO₂ surface ice grain size distributions for the asymmetric retraction period corresponding to four MRO planning cycles used to prepare Figure 3 mosaics.

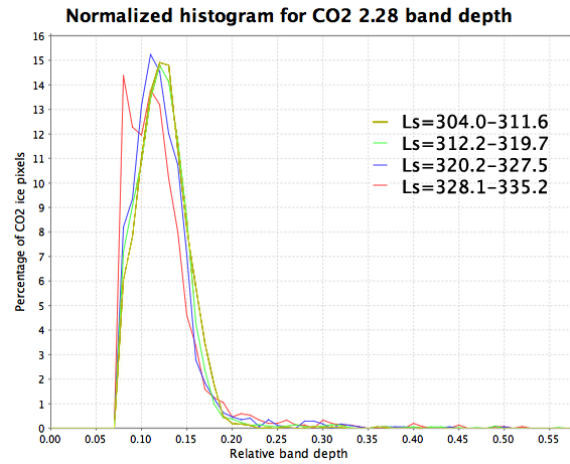
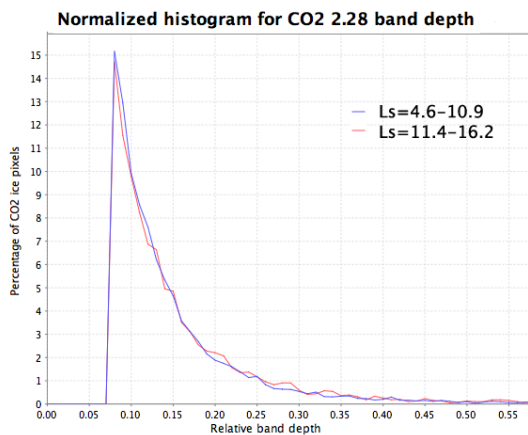


Figure 7.4 Histograms showing CO₂ surface ice grain size distributions for the stable period corresponding to four MRO planning cycles used to prepare Figure 3 mosaics



< Figure 7.5 Histograms showing CO₂ surface ice grain size distributions for the recondensation period corresponding to two MRO planning cycles used to prepare Figure 3 mosaics.

DISCUSSION

Interpretation of Seasonal Mosaics

Based on the spatial extent and rate of sublimation or condensation, we divide our discussion of the seasonal mosaics into five major phases – presublimation, cryptic, retraction, stable and recondensation phases. The first phase, from $L_s=160-200$ we term *presublimation* phase. From $L_s=200-240$, is the appearance of the *cryptic* region, from $L_s=240-290$ is the cap *asymmetric retraction* phase and from $L_s=290-340$ is the *stable* cap phase. These phases are indicated on Figure 7. Following $L_s=340$, CRISM MSP coverage is spotty, though it is clear from Figure 7 that CO_2 has reappeared and extends further equatorward than $80^\circ S$ at $L_s=4-10$. This CO_2 is most likely the growing surficial cap, as discussed in more depth below.

Presublimation phase ($L_s=160-200$). Figures 3.1-3.2 cover this phase. The CO_2 seasonal cap clearly extends equatorward of $60^\circ S$, with relatively low, homogenous albedo and the cryptic region is not readily visible.

The edge of the CO_2 seasonal cap displays a decrease in the strength of the $1.435\mu m$ CO_2 absorption band as shown in the middle column of Figure 3.1 and 3.2. This decrease in CO_2 band strength could be due to a decrease in area covered by the CO_2 cap (at fractions of the $\sim 187.5m$ scale) or due to a decrease in the grain size as the edge of the cap is sublimating. These two effects are not separable without high resolution images of the cap edge. The edge of the cap thus defined forms an annulus around 10-100km wide around the retreating cap.

H₂O ice clouds from $L_s=160-200$. H_2O ice is also present over the $60-80^\circ S$ latitude range, encircling the geographic pole. These H_2O ice pixels display low H_2O ice grain index ratios (Eq. 4), therefore we interpret this water ice as polar vortex clouds originating from the Hellas region (Haberle et al., 1979). There is a large decrease in the area covered by water ice around $L_s\sim 200$.

It is unclear what relationship exists between the water ice clouds that are dominant prior to $L_s=200$ and the subsequent weaker water ice detections on the seasonal cap, mostly in the cryptic region, after $L_s=200$. It is possible that the water ice clouds may condense on cryptic region after $L_s=200$, however it is also possible the ice clouds move equatorward and are carried out of the polar region as the springtime recession begins.

Probable H₂O surface deposits after $L_s=200$. Water ice detections near $75^\circ S$, $250^\circ E$ after $L_s=200$ are likely surface deposits, for four reasons – 1.) they do not show low H_2O ice grain indexes as per Eq. 4, therefore they are not likely to contain fine-grained water ice, 2.) they persist in the same location from $L_s=205-225$, 3.) this area is associated with the western edge of the 105km diameter Lau

crater (74.2°S,252.2°E) and 4.) the MARCI images (particularly the $L_s=211$ image) show a low albedo patch on the steep western side of Lau. In addition, water ice detections at 84°S, 151°E and 85°S, 60°E are also candidates to be surface deposits since they lie around the edge of the SPRC plateau. Due to large grained CO₂ ice around the SPRC plateau, the H₂O grain size index (Eq. 4) cannot be employed to determine the H₂O grain size. These H₂O deposits have disappeared by $L_s=230-240$.

Probable H₂O clouds after $L_s=200$. Spatially coherent water ice detections near 70-75°S from 90-210°E persist over $L_s=200-225$, and are probably vestiges of the cloud system that is dominant prior to $L_s=200$, since some display low H₂O ice grain size indexes (Eq. 4). It should be noted that MARCI images show no visible evidence for ice clouds, suggesting the clouds are tenuous.

Cryptic phase ($L_s=200-240$). Figures 3.2-3.3 cover this phase. The MARCI images clearly show the rapid appearance of the Cryptic Region from $L_s=195-210$, and the CRISM ice maps show evidence of pure water ice appearing in the Cryptic Region at that time. The water ice that appears in the Cryptic Region can be seen to follow topography, this is especially clear in $L_s=209-216$ when the rim of Ultimum Chasma (at 81°S, 150°E) is outlined by pixels where only H₂O ice is detected. There is no clear indication of low H₂O ice grain size index (Eq. 4) associated with the H₂O ice spectral signatures in the Cryptic Region from $L_s=200-240$, therefore they are likely to be due to surface water ice deposits as suggested by some researchers (Bibring et al., 2004; Titus, 2005b). Promethei Chasma (above Ultimum Chasma in the polar stereographic representation in Figure 3) shows a mixture of CO₂ and H₂O ice signatures at the same time period.

Most of the water ice in the Cryptic Region disappears during the $L_s=200-240$ time period, and it is around this time that there is a peak of 25 pr- μm and an average around 20pr- μm (from a baseline of $\sim 5\text{pr-}\mu\text{m}$) in water vapor in the southern latitudes (Smith et al., this issue). It seems reasonable to suggest the water ice from the Cryptic Region is the source of this spike in atmospheric water vapor. Alternately, other researchers have suggested H₂O ice beneath the SPRC plateau may be the source of an increase in water vapor during this time (Titus et al., 2008).

The Cryptic Region is roughly 1.7 million km² at its greatest extent (using calculations based on the low albedo region in the MARCI image at $L_s=211$). Based on CRISM observations at $L_s=209.4-216.1$, roughly two-thirds of the Cryptic Region shows signs of water ice (~ 1.1 million km²). If all of the water in the south polar peak in the atmosphere was sourced from the Cryptic Region, and if the area covered by the atmospheric peak is roughly 17 million km² (this assumes the above-baseline H₂O vapor region covers 35°S-75°S degrees in latitude), and assuming the water was sourced from a homogenous, pure, single layered deposit, then the layer of water ice would be roughly 230 microns ((20-

5)*(17/1.1)) thick. This is obviously a simplification of the true situation, but it gives a testable hypothesis for future models and observations.

Asymmetric Retraction phase ($L_s=240-290$). Figures 3.3-3.4 cover this phase. The bright albedo feature (the “Mountains of Mitchel”) at 70°S , 30°E is clearly visible in the MARCI images from $L_s=230-270$, and although CRISM coverage extends definitively over this feature only at $L_s=261-267$, it clearly shows the signature of fine grained CO_2 ice.

This phase of the cap retreat is almost entirely devoid of water ice detections. The last vestiges of water ice are detected at $L_s=243-251$ at 83°S , 125°E . This location is at the end of Promethei and Ultimum Chasmata and is a hot spot of water activity after the retraction of water ice clouds at $L_s=205-250$. It was also recognized in MY 27 by OMEGA and disappeared at $L_s=254$ (paragraph [58] of Langevin et al., 2007). No water ice deposits are detected near 156°E , 86.4°S at $L_s=270$, as reported by Titus (2005b), however this may be due to lack of coverage or interannual variability. The absence of ice lags at $L_s=270$ may be due to 1.) subpixel mixing of remnant CO_2 ice and dust (Titus et al., 2008), or 2.) elevated atmospheric temperatures or surface obscuration caused by the planet encircling dust event which occurred around $L_s=270$ in MY28.

Stable phase ($L_s=290-340$). Figures 3.5-3.6 cover this phase. The most extensive CRISM coverage of the SPRC was collected from $L_s=312-320$. It is difficult to make out at the resolution of Figure 3, but from $L_s=312-342$ CRISM detects small deposits of water ice from $270-360^\circ\text{E}$, in much the same location as identified from THEMIS data and shown in Figure 3 of Piqueux et al. (2008). Prior to $L_s=312$, only CO_2 ice is detected in these locations.

Recondensation phase ($L_s=340-040$). Figures 3.6-3.7 cover this phase. CRISM and MARCI coverage for this time is spotty due to low solar illumination conditions at this time. The CO_2 index map indicates that CO_2 has reappeared and extends further equatorward than 80°S at $L_s=4-10$ approximately symmetrically around the geographic pole. GCM simulations predict the condensation of CO_2 ice to begin around $L_s=0-10$ (Haberle et al., 2004), as the cap cools at the start of southern fall - this is in accord with our observations here. MOLA derived CO_2 deposition estimates also suggest symmetric deposition around the geographic pole (Smith et al., 2009), which is also supported by our observations. MARCI images are more ambiguous and do not show obvious signs of the deposition of CO_2 ice, due probably due to the lack of coverage over the pole itself and the very thin nature of the deposit at this time. CRISM observations show no difference in the grain size or albedo of the Cryptic Region up to $L_s=16.2$, therefore it is possible that whatever process differentiates the Cryptic Region from the rest of the CO_2 seasonal cap has not manifested itself by $L_s=16$.

We investigated several CRISM MSP images at this time and found evidence of the CO₂ condensation process. Figure 8 shows part of MSP 00009624_01, centered at 70°E, 67°S and obtained at L_s=11.7. This image shows an increase in albedo over the newly condensing cap, and typical ice cap features such as wind blown dark areas where the CO₂ ice has been stripped from some areas. An example spectrum of the CO₂ ice cap is also shown - the spectra of the high albedo areas show fine-grained CO₂ ice, as determined by the shallow absorption features at 2.28μm.

Comparison to TES observations of MY 23 recession. Kieffer et al. (2000) showed that limited thermal infrared coverage by TES over the Cryptic Region at L_s=12 and over the geographic pole at L_s=25 was not able to detect the recondensation of fine grained CO₂ frost. Kieffer et al. postulated that transparent slab ice was forming at that time, based on the nearly constant brightness temperature over the 250-500cm⁻¹ spectral range of an average of 60 TES spectra. However, CRISM observations during MY28 show evidence for fine grained ice, and in addition no differences in grain size are detected over the Cryptic Region (see in particular the observations of 1.435 μm depth at L_s=4.6-10.9). This result is difficult to reconcile with TES observations, although one possibility is that the CO₂ ice coverage is sufficiently thin at this stage that its effect on the 250-500 cm⁻¹ region is negligible and TES is mostly sensing the soil beneath the ice. The nature of the early CO₂ condensation process clearly requires further study.

Comparisons to THEMIS high resolution atmospheric observations. Inada et al. (2007) used high resolution THEMIS images to observe 'trough clouds' with heights of around 600m in topographic lows around the south polar cap from L_s=251-320 in MY26. No detections of water ice clouds were made in trough regions in the L_s=251-320 by CRISM in MY28. Inada et al. do not have data covering periods earlier than L_s=240. Although it is possible some pre-L_s=251 water ice detections in topographic lows may be associated with



Figure 8. Evidence for CO₂ seasonal cap recondensation at L_s=11.7. (left) part of image MSP00009624_01, centered at 70E, 67S. The image shows the spectral band at 1.079μm. (right) MSP spectrum from pixel at x=52, y=2351 showing CO₂ absorption features at 2.28 μm. The image is 10km wide and north is up.

fogs or ground-hugging clouds, most topographic water ice detections are not associated with low H₂O ice grain size index ratios (Eq. 4) making surface deposits a more likely explanation for these water ice signatures.

Comparison to OMEGA observations of MY27 recession. OMEGA detected water ice clouds over Hellas at L_s=140-154 (Figure 12c of Langevin et al., 2007) but due to the elliptical orbit of Mars Express, OMEGA did not return to observe the south polar cap until L_s=183.9-192.5, when it detected low amounts of water ice over the seasonal cap, with a 'dry spoke' along 60°E longitude, in the direction of Hellas. Our results expand upon this OMEGA observation, bringing the detection of spatially coherent water ice clouds to earlier in the year - at least to L_s=167.9 and perhaps earlier to L_s=161.9 (although coverage at L_s=161.9 is sparse). Our observations also place a large reduction in water ice cloud coverage at L_s=200-204, and further, we resolve the clouds as extending off the cap at latitudes of ~56-58°S between longitudes 90-150°E from L_s=167-199, into the Promethei Terra region south east of Hellas.

Interpretation of CO₂ Grain Size Results

Figures 7.1-7.5 show the histograms for derived seasonal CO₂ ice grain sizes. Although the patchy coverage of the polar regions frustrates definitive "pole-wide" knowledge about grain size estimates, we make the assumption that our observations are representative of the rest of the polar cap at the time of observation.

Despite the limitations of our CO₂ ice grain size modeling (which assumes 100% coverage of pure CO₂ ice with no dust cover, leading to 'minimum apparent' grain size estimates), the histograms show that the range of grain sizes across the CO₂ ice cap is relatively restricted according to the phase the cap is in (at least at the ~187.5m spatial scale).

Pre-sublimation CO₂ ice grain sizes. From L_s=162-208, the range of relative 2.28 μm band depths of CO₂ ice is at its widest. During this period, the largest relative band depth of 0.535 are achieved at L_s=191-199. Assuming they are due to CO₂ alone and our models are correct, this would correspond to minimum apparent grain sizes slightly less than 7±1cm.

Cryptic period CO₂ ice grain sizes. As spring begins to warm up the south polar region (from L_s=209-267) the grain sizes adopt a more restricted profile, becoming smaller (the largest band depths now range from 0.3-0.4 relative band depth, corresponding to a grain size of 2-3cm), and with a peak just short of 0.2 relative band depth (suggesting most of the CO₂ ice grains sizes cluster around an average of 5-10±1mm).

Asymmetric retraction period CO₂ ice grain sizes. During L_s=271-303, relative bands depth profiles for CO₂ ice continue to constrict. The maximum band depths of 0.25 (corresponding to a grain size of 10±1mm) and most of the CO₂ ice relative band depths are around 0.1-0.2 (corresponding to a grain sizes of 2.5-7.5±1mm).

Stable period CO₂ ice grain sizes. During the summer stable period, the relative band depths are also the most stable and constricted. Practically all of the relative band depths are below 0.2 (grain size of 7.5±1mm) and most cluster around the 0.1-0.15 relative band depth (corresponding to a grain size of 2.5-5±1mm).

Recondensation period CO₂ ice grain sizes. During the recondensation period, the relative band depths are also extremely stable, but a prominent histogram peak is not seen above the threshold (the highest number of pixels have grain sizes at the threshold, suggesting the peak is below the threshold and therefore not shown on the histogram). This is most likely because the majority of CO₂ ice grain sizes are below our threshold (0.07 relative band depth, corresponding to 1.2mm CO₂ ice grains, according to our spectral models). The lack of larger grained ice is directly related to the fact that the SPRC is not imaged in these sequences, and only fine-grained CO₂ from the condensing cap is detected. The small number of pixels that are identified as CO₂ ice makes the histograms more sensitive to noisy pixels, and they display a long tail of relative band depths. We interpret these histograms as showing no prominent mode of grain sizes and suggest that most of the CO₂ ice grain sizes are below 1.2mm at this time.

Interpretations of decreasing of CO₂ ice grain sizes. During the L_s=200-310 springtime period, the SPRC is covered by our observations and the maximum grain sizes of the residual polar cap are clearly decreasing. This observation might be explained in two ways: 1.) by relatively small subliming grains of CO₂ ice being transported poleward and getting cold trapped on the SPRC as fine-grained deposits (Kieffer et al., 2000) or 2.) by CO₂ ice grains sublimating and decreasing in size in place on the SPRC. Both options could explain our observation, and this process requires further study.

One interpretation of the peaks in CO₂ ice grain size histograms (combined with CO₂ abundance maps in Figure 3) is that the SPRC CO₂ ice is responsible for the maximum relative band depths in each histogram. In early pre-sublimation CRISM observations the SPRC CO₂ ice grains experience growth conditions until L_s=190 when grain sizes of ~7cm are reached, and over summer these grains lose mass/sublime or are covered by finer grains until they display a stable size during summer (L_s=310) of ~5mm.

Comparison with previous grain size results. The first grain size estimations for CO₂ in the south pole of Mars came from studies of the Mariner 7 IRS dataset

covering the SPRC at $L_s=200$. This study suggested quite large (millimeter to centimeter sized) grains (Calvin, 1990; Calvin and Martin, 1994).

OMEGA observations at $L_s=142$ uncovered “slab ice” at 59S, 344E, which was modeled to indicate grain sizes of 30cm (Langevin et al., 2007). CRISM did not observe this region at $L_s=142$. We found that CO_2 grain sizes were larger on the SPRC than on the seasonal cap, which was also reported by Kieffer et al. (2000) and Langevin et al. (2007). Our minimum apparent grains size estimates of $\sim 7\pm 1$ cm for grains on the SPRC at $L_s=190$ are similar to OMEGA (5-10cm, paragraph [39] and [58] of Langevin et al., 2007 and page 17 of Doute et al., 2007 - at $L_s=335-348$) and TES (~ 10 cm, $L_s=193$ on perennial cap, Figure 3 caption of Kieffer et al., 2000). Kieffer also reports that the grain size decreases by the summer ($L_s=316$, Figure 3b of Kieffer et al., 2000). This is in broad accordance with our observations.

The results reported here for CRISM data are in reasonable agreement with those of Glenar et al., (2005) who found telescopic spectra of the bright regions of the south polar cap at $L_s=231$ were well modeled by CO_2 ice with a grain size of 13mm (this is just above our average grain size of $5-10\pm 1$ mm for this period), and Hansen et al., (2005) who suggested PFS observations of the SPRC at $L_s=330$ were well modeled by a surface containing CO_2 ice of grain size 5-10mm (this is just above our average of $2.5-5\pm 1$ mm for the stable phase).

The grain size estimates presented here are in broad accordance with those of Doute et al. (2006) and Langevin et al. (2007) despite the fact that we have used a different grain size estimate method, and we have made no assumptions about contamination by dust or water ice. All of the Doute et al. models of the SPRC use 400-1600ppm H_2O with 300-400 μm grain size, which could be appropriate for late summer observations.

CO₂ slab ice in the Cryptic Region. CRISM data provide no evidence for CO_2 slab ice, or any large grained CO_2 ice (no relative band depths for 2.28 μm band of greater than ~ 0.16 corresponding to grain sizes of ~ 5 mm) in the Cryptic Region, in agreement with the results reported by the OMEGA team (Langevin et al., 2007). In fact, the Cryptic Region, even before it shows Cryptic behavior (before $L_s=190$) is characterized by an absence of CO_2 features. However, CO_2 ice clearly controls the temperature of the surface, as determined by the thermal infrared observations of TES (Kieffer et al., 2000). One explanation is that a layer of dust on the surface of the Cryptic Region lies on top of the CO_2 ice slab, in thermal equilibrium with CO_2 ice beneath (Titus et al., 2008). Langevin et al. presented spectral models that require the dust to be in the top 2mm of the surface (Langevin et al., 2006). The dust must be heavy enough to mask the CO_2 slab from detection in the VNIR, however it must be thin or discontinuous enough to allow radiation to penetrate and power the Cryptic Region cold jets, as has been proposed in Kieffer’s standard cold jet model (Kieffer et al., 2006). An additional explanation for the lack of large path length CO_2 absorption features is

that all photons in VNIR wavelengths entering the transparent CO₂ ice slab would be absorbed, leaving the only signature returned to the sensor that due to the top layer of dust.

CONCLUSIONS

We have presented the results of CRISM and MARCI mapping during the first Mars year of Mars Reconnaissance Orbiter science mapping operations.

The observations reported herein have for the first time:

1.) mapped latitudinal/longitudinal extent of spatially coherent water ice clouds above the polar cap from $L_s=160-200$. These clouds may be used as tracers of atmospheric dynamics, including possible indications of east-west asymmetry in weather patterns (Brown et al., 2008b).

2.) within the Cryptic Region, uncovered the presence of H₂O ice with no accompanying CO₂ ice signatures. These identifications are an intriguing part of the Cryptic Region puzzle. If ice sourced from the Cryptic Region is solely responsible for the summertime rise in water vapor in the southern hemisphere, Cryptic Region water ice deposits may form a layer more than 200 microns thick.

3.) within the Cryptic Region, mapped areas at the $\sim 187.5\text{m/pixel}$ scale where no CO₂ or H₂O ice was observed (due either to obscuration by dust or sublimation of the icy volatiles).

4.) mapped the seasonal variations in the strength of the $2.28\ \mu\text{m}$ CO₂ absorption relative band depth, and inferred that CO₂ ice grains and apparent grain sizes of up to $\sim 7\pm 1\text{cm}$ are present prior to the springtime sublimation of the south polar cap, compared with average grain sizes of $2.5-5\pm 1\text{mm}$ in the stable summer time residual polar cap.

5.) mapped the recondensation of the CO₂ seasonal cap from $L_s=0-30$ and provided evidence of a very thin, fine-grained deposit that extends beyond 80°S by $L_s=4-10$. The deposit is roughly symmetrical around the geographic pole. Whatever process is responsible for forming the Cryptic Region is not apparent before $L_s=16$, since no difference in grain size or albedo (from the rest of the condensing cap) is observed in that region up to that time.

ACKNOWLEDGEMENTS

We would like to thank the entire CRISM Team, particularly the Science Operations team at JHU APL, and also the MARCI PI (Mike Malin) and his staff. We thank Sylvain Piqueux and an anonymous reviewer for their helpful guidance. We thank Ted Roush for supplying optical constants for palagonite. Special thanks to Tim Titus, Mike Wolff, Yves Langevin and Todd Clancy for illuminating discussions. This investigation was partially funded by NASA Grant NNX08AL09G.

REFERENCES

- Benson, J. L., James, P. B., 2005. Yearly comparisons of the martian polar caps: 1999–2003 Mars Orbiter Camera observations. *Icarus* 174, 513-523.
- Bibring, J.-P., Langevin, Y., Poulet, F., Gendrin, A., Gondet, B., Berthe, M., Soufflot, A., Drossart, P., Combes, M., Bellucci, G., Moroz, V., Mangold, N., Schmitt, B., 2004. Perennial water ice identified in the south polar cap of Mars. *Nature* 428, 627-630.
- Bohren, C. F., 1987. Multiple scattering of light and some of its observable consequences. *American Journal of Physics* 55, 524-533.
- Brown, A. J., 2006. Spectral Curve Fitting for Automatic Hyperspectral Data Analysis. *IEEE Transactions on Geoscience and Remote Sensing* 44, 1601-1608. <http://arXiv.org/abs/1401.5562>
- Brown, A. J., Byrne, S., Tornabene, L. L., Roush, T., 2008a. Louth Crater: Evolution of a layered water ice mound. *Icarus* 196, 433-445. <http://arXiv.org/abs/1401.8024>
- Brown, A. J., Hollingsworth, J. L., Kahre, M. A., Haberle, R. M., 2008b. Pre-recessional (Ls 160-200) Polar Water Ice Clouds at the Martian South Pole: Potential Tracer of East-West Asymmetry? Fall AGU, San Francisco, CA, AGU, Abstract P11A-1253.
- Brown, A. J., Storrie-Lombardi, M. C., 2006. MR PRISM - A spectral analysis tool for the CRISM. *Proceedings of SPIE Optics and Photonics*, San Diego, CA, SPIE, Abstract 28. <http://arXiv.org/abs/1401.7089>
- Brown, A. J., Wiseman, S., McGuire, P., Wolff, M., Smith, M., 2007. Mars: South Polar Spring Recession as observed by CRISM. *Eos Trans. AGU*, San Francisco, CA, AGU, abstract P33A-1016.
- Calvin, W. M., 1990. Additions and corrections to the absorption coefficients of CO₂ ice - Applications to the Martian south polar cap. *Journal of Geophysical Research* 95, 14743-14750.
- Calvin, W. M., Martin, T. Z., 1994. Spectral variability in the seasonal south polar cap of Mars. *Journal of Geophysical Research* 99, 21143-21152.
- Clancy, R. T., Sandor, B. J., Wolff, M. J., Christensen, P. R., Smith, M. D., Pearl, J. C., Conrath, B. J., Wilson, R. J., 2000. An intercomparison of ground-based millimeter, MGS TES, and Viking atmospheric temperature measurements: Seasonal and interannual variability of temperatures and dust loading in the global Mars atmosphere. *Journal of Geophysical Research-Planets* 105, 9553-9571.
- Colaprete, A., Toon, O. B., 2002. Carbon dioxide snow storms during the polar night on Mars. *Journal of Geophysical Research* 107.
- Conrath, B. J., 1975. Thermal structure of the Martian atmosphere during the dissipation of the dust storm of 1971. *Icarus* 24, 36-46.
- Doute, S., Schmitt, B., Langevin, Y., Bibring, J.-P., Altieri, F., Bellucci, G., Gondet, B., Poulet, F., 2006. South Pole of Mars: Nature and composition of the icy terrains from Mars Express OMEGA observations. *Planetary and Space Science* 55, 113-133.
- Feldman, W. C., Prettyman, T. H., Boynton, W. V., Murphy, J. R., Squyres, S., Karunatillake, S., Maurice, S., Tokar, R. L., McKinney, G. W., Hamara, D. K., Kelly, N., Kerry, K., 2003. CO₂ frost cap thickness on Mars during northern

- winter and spring. *Journal of Geophysical Research* 108, doi:10.1029/2003JE002101.
- Giuranna, M., Formisano, V., Grassi, D., Maturilli, A., 2007. Tracking the edge of the south seasonal polar cap of Mars. *Planetary and Space Science* 55, 1319-1327.
- Glenar, D. A., Hansen, G., BJORAKER, G., Smith, M., Pearl, J., Blaney, D., 2005. Bright-region radiative properties within the Mars south polar cap (Ls=231) from near-infrared spectroscopic imaging. *Icarus* 174, 600-603.
- Guo, X., Lawson, W. G., Richardson, M. I., Toigo, A., 2009. Fitting the Viking lander surface pressure cycle with a Mars General Circulation Model. *Journal of Geophysical Research* 114, doi://10.1029/2008JE003302.
- Haberle, R. M., Leovy, C. B., Pollack, J. B., 1979. A numerical model of the Martian polar cap winds. *Icarus* 39, 151-183.
- Haberle, R. M., Mattingly, B., Titus, T. N., 2004. Reconciling different observations of the CO₂ ice mass loading of the Martian north polar cap. *Geophysical Research Letters* 31, doi:10.1029/2004GL019445.
- Hansen, G., Giuranna, M., Formisano, V., Fonti, S., Grassi, D., Hirsh, H., Ignatiev, N., Maturilli, A., Orleanski, P., Piccioni, G., Rataj, M., Saggini, B., Zasova, L., 2005. PFS-MEX observation of ices in the residual south polar cap of Mars. *Planetary and Space Science* 53, 1089-1095.
- Hansen, G. B., 1997. The infrared absorption spectrum of carbon dioxide ice from 1.8 to 333mm. *Journal of Geophysical Research* 102, 21569-21587.
- Hansen, G. B., 2005. Ultraviolet to near-infrared absorption spectrum of carbon dioxide ice from 0.174 to 1.8 μ m. *Journal of Geophysical Research* 110, E11003.
- Hess, S. L., Henry, R. M., Leovy, C. B., Ryan, J. A., Tillman, J. E., 1977. Meteorological Results From the Surface of Mars: Viking 1 and 2. *Journal of Geophysical Research* 82, 4559-4574.
- Hess, S. L., Henry, R. M., Tillman, J. E., 1979. The seasonal variation of atmospheric pressure on Mars as affected by the south polar cap. *Journal of Geophysical Research* 84, 2923-2927.
- Hess, S. L., Ryan, J. A., Tillman, J. E., Henry, R. M., Leovy, C. B., 1980. The annual cycle of pressure on Mars measured by Viking landers 1 and 2. *Geophysical Research Letters* 7, 197-200.
- Hinson, D. P., Wilson, R. J., 2002. Transient eddies in the southern hemisphere of Mars. *Geophysical Research Letters* 29, doi:10.1029/2001GL014103.
- Inada, A., Richardson, M. I., McConnochie, T. H., Strausberg, M. J., Wang, H., Bell III, J. F., 2007. High-resolution atmospheric observations by the Mars Odyssey Thermal Emission Imaging System. *Icarus* 192, 378-395.
- James, P. B., Briggs, G., Barnes, J., Spruck, A., 1979. Seasonal recession of Mars' south polar cap as seen by Viking. *Journal of Geophysical Research* 84, 2889-2992.
- James, P. B., Malolepszy, K. M., Martin, L. J., 1987. Interannual variability of Mars' south polar cap. *Icarus* 71, 298-305.
- James, P. B., Thomas, P. C., Wolff, M. J., Bonev, B. P., 2007. MOC observations of four Mars year variations in the south polar residual cap of Mars. *Icarus* In Press, Corrected Proof, doi:10.1016/j.icarus.2007.07.014
- Kieffer, H., 1990. H₂O grain size and the amount of dust in Mars' residual north polar cap. *Journal of Geophysical Research* 95, 1481-1493.

- Kieffer, H. H., Christensen, P. R., Titus, T. N., 2006. CO₂ jets formed by sublimation beneath translucent slab ice in Mars' seasonal south polar ice cap. *Nature* 442, 793-796.
- Kieffer, H. H., Titus, T. N., Mullins, K. F., Christensen, P. R., 2000. Mars south polar spring and summer behavior observed by TES: Seasonal cap evolution controlled by frost grain size. *Journal of Geophysical Research-Planets* 105, 9653-9699.
- Langevin, Y., Bibring, J.-P., Montmessin, F., Forget, F., Vincendon, M., Douté, S., Poulet, F., Gondet, B., 2007. Observations of the south seasonal cap of Mars during recession in 2004–2006 by the OMEGA visible/near-infrared imaging spectrometer on board Mars Express. *Journal of Geophysical Research* 112, 10.1029/2006JE002841.
- Langevin, Y., Douté, S., Vincendon, M., Poulet, F., Bibring, J.-P., Gondet, B., Schmitt, B., Forget, F., 2006. No signature of clear CO₂ ice from the 'cryptic' regions in Mars' south seasonal polar cap. *Nature* 442, 790-792.
- Malin, M. C., Bell, J. F., Calvin, W., Clancy, R. T., Haberle, R. M., James, P. B., Lee, S. W., Thomas, P. C., Caplinger, M. A., 2001. Mars Color Imager (MARCI) on the Mars Climate Orbiter. *Journal of Geophysical Research-Planets* 106, 17651-17672.
- Montmessin, F., Bertaux, J.-L., QuÉmerais, E., Korablev, O., Rannou, P., Forget, F., Perrier, S., Fussen, D., Lebonnois, S., RÈbÈrac, A., Dimarellis, E., 2006. Subvisible CO₂ ice clouds detected in the mesosphere of Mars. *Icarus* 183, 403-410.
- Murchie, S., Arvidson, R., Bedini, P., Beisser, K., Bibring, J.-P., Bishop, J., Boldt, J., Cavender, P., Choo, T., Clancy, R. T., Darlington, E. H., Des Marais, D., Espiritu, R., Fort, D., Green, R., Guinness, E., Hayes, J., Hash, C., Heffernan, K., Hemmler, J., Heyler, G., Humm, D., Hutcheson, J., Izenberg, N., Lee, R., Lees, J., Lohr, D., Malaret, E., T., M., McGovern, J. A., McGuire, P., Morris, R., Mustard, J., Pelkey, S., Rhodes, E., Robinson, M., Roush, T., Schaefer, E., Seagrave, G., Seelos, F., Silverglate, P., Slavney, S., Smith, M., Shyong, W.-J., Strohbehn, K., Taylor, H., Thompson, P., Tossman, B., Wirzburger, M., Wolff, M., 2007. Compact Reconnaissance Imaging Spectrometer for Mars (CRISM) on Mars Reconnaissance Orbiter (MRO). *Journal of Geophysical Research* 112, E05S03, doi:10.1029/2006JE002682.
- Pettengill, G. H., Ford, P. G., 2000. Winter Clouds Over the North Martian Polar Cap. *Geophysical Research Letters* 27, 609–612.
- Piqueux, S., Christensen, P. R., 2008. Deposition of CO₂ and erosion of the Martian south perennial cap between 1972 and 2004: Implications for current climate change. *Journal of Geophysical Research* 113, doi:10.1029/2007JE002969.
- Piqueux, S., Edwards, C. S., Christensen, P. R., 2008. Distribution of the ices exposed near the south pole of Mars using Thermal Emission Imaging System (THEMIS) temperature measurements. *Journal of Geophysical Research* 113, doi:10.1029/2007JE003055.
- Schott, J. R., 1996. *Remote Sensing: The Image Chain Approach*. Oxford University Press, New York NY.

- Shkuratov, Y., Starukhina, L., Hoffmann, H., Arnold, G., 1999. A Model of Spectral Albedo of Particulate Surfaces: Implications for Optical Properties of the Moon. *Icarus* 137, 235-246.
- Smith, D. E., Zuber, M. T., Neumann, G. A., 2001. Seasonal variations of snow depth on Mars. *Science* 294, 2141-2146.
- Smith, D. E., Zuber, M. T., Torrence, M. H., Dunn, P. J., Neumann, G. A., Lemoine, F. G., Fricke, S. K., 2009. Time variations of Mars' gravitational field and seasonal changes in the masses of the polar ice caps. *Journal of Geophysical Research* 114, doi:10.1029/2008JE003267.
- Titus, T. N., 2005a. Mars Polar Cap Edges Tracked over 3 full Mars years. LPSC XXXVI, Houston, TX, LPI, Abstract 1993.
- Titus, T. N., 2005b. Thermal infrared and visual observations of a water ice lag in the Mars southern summer. *Geophysical Research Letters* 32, doi:10.1029/2005GL024211.
- Titus, T. N., Calvin, W. M., Kieffer, H. H., Langevin, Y., Prettyman, T. H., Martian polar processes. In: J. F. Bell, (Ed.), *The Martian Surface: Composition, Mineralogy, and Physical Properties*. Cambridge University Press, 2008.
- Titus, T. N., Kieffer, H. H., Christensen, P. R., 2003. Exposed water ice discovered near the south pole of Mars. *Science* 299, 1048-1051.
- Tobie, G., Forget, F., Lott, F., 2003. Numerical simulation of the winter polar wave clouds observed by Mars Global Surveyor Mars Orbiter Laser Altimeter. *Icarus* 164, 33-49.
- Wood, S. E., Paige, D. A., 1992. Modeling the Martian seasonal CO₂ cycle 1. Fitting the Viking Lander pressure curves. *Icarus* 99, 1-14.